Journal of Visualization, Vol. 3, No. 1 (2000) 51-61

Observation of Nonequilibrium Radiation behind Strong Shock Waves in Low-density Air

Morioka, T.*, Sakurai, N.*, Maeno, K*. and Honma, H.*

* Graduate School of Science and Technology, Chiba University, 1-33, Yayoi-cho, Inage-ku, Chiba 263-8522, Japan.

Received 1 June 1999.
Revised 20 August 1999.

***Abstract*:** Nonequilibrium radiation phenomena behind strong shock waves in low-density air are observed by using a couple of CCD camera systems in a shock tube experiment. The simultaneous observation for total radiation and its spectral radiation is carried out in order to elucidate space-dependent contribution of an individual radiation spectrum to the total radiation intensity. The results are shown for the shock velocity range from 9.0 km/s to 12.1 km/s at the initial pressure 13.3 Pa. Wavelength range is selected from 300 nm to 445 nm to investigate mainly the contributions from UV radiation. It is found that the band spectra due to the molecular species N_2^+ and CN mainly contribute to the first-peak, while the spectra due to the atomic species O^+ and N mainly contribute to the formation of the second-peak. It is also found that the Balmer series in H spectra strongly contributes to the second-peak. The radiation along the tube wall surfaces is composed of the same constituents as those around the tube axis as well as the spectra coming from the impurities.

***Keywords*:** strong shock wave, radiation, spectroscopy.

1. Introduction

In the heating problem of space vehicles reentering onto the atmosphere, great efforts have been made to understand high-enthalpy flows. When the reentry velocity exceeds 10 km/s, radiative heating from the shocked air ahead of the vehicle plays an important role for the heat flux to the wall surface as well as convective heating.

In order to clarify the radiative characteristics of the shocked air, experimental studies have been carried out during the last decade by many investigators using shock tube facilities (Honma and Iizuka, 1991; Sharma and Gillespie, 1991; Sharma, 1993). The techniques for radiation observation in shock tube experiments have been limited for a long time within such a few means as photomultipliers, rotating cameras and so on. However, recent technical developments of high-speed photography and photonics make it possible to explore a new system for observing radiation phenomena of the shocked air.

Recently, a CCD camera system was introduced into radiation observation of strong shock waves in low-density air (Koreeda et al., 1996; Koreeda et al., 1998). The system consists of an imaging spectrograph, a streak camera, a gated image-intensified CCD camera and a personal computer. Some interesting features were obtained, independently, for the total radiation and for the spectral radiation behind strong shock waves in air above 10 km/s velocity (Honma et al., 1996; Morioka et al., 1997). The observations using an analogous technique were also conducted by Dumitrescu et al. (1997). Their observations were made in mixtures as $N_2/CH_4/Ar$, CO_2/N_2 and so on in relation to the reentry into Titan and Martian atmospheres. In relation to a sample return mission of a near-earth asteroid (MUSES-C), which is currently programmed by The Institute of Space and Astronautical Science, spatial distribution of emission spectra of the shock front in air was obtained by means of one-dimensional imaging spectroscopy (Fujita et al., 1997; Fujita et al., 1998).

The present paper describes the simultaneous observation for the total radiation and its spectral radiation are carried out by using a couple of CCD camera systems, since it is necessary to elucidate the space-dependent contributions of an individual radiation spectrum to the total radiation intensity for nonequilibrium radiation behind strong shock wave in low-density air. In the present paper, our attention is focused on the formation of 2-peaks profile of total radiation intensity, which occurs as the shock velocity exceeds 11 km/s at the initial pressure 13.3 Pa.

2. Experimental Apparatus and Diagnostic System

Figure 1 shows a configuration of the free-piston, double-diaphragm shock tube which is used to generate strong shock waves in low-density air (Honma, 1993). The cross section of low-pressure tube is 40 mm × 40 mm square. The observation window of test section is made from quartz for transparency over the UV radiation range, and its viewable area is 40 mm × 150 mm rectangular for taking a two-dimensional image of radiation.

Figure 2 shows a layout of diagnostic system for simultaneously observing the total radiation and its spectral radiation behind a strong shock wave by the coupled use of a pair of CCD camera systems. The two-dimensional, time-frozen total radiation is observed by the system of left hand side of the shock tube, and the space-resolved spectral radiation at a point of the tube axis of shock tube is observed by the system of right hand side.

The former system consists of a UV camera lens, a gated image-intensified CCD camera (ICCD), a delay/pulse generator and a personal computer. The UV camera lens is Nikon, model UV-Nikkor 105 mm F4.5S. This camera lens consists of a set of 6 lenses chosen to provide low degrees of astigmatism and wavelength aberration. The ICCD is Hamamatsu Photonics, model C5987, whose two-dimensional diode array is composed by 512 × 512 square pixels of 12 μm × 12 μm, each pixel producing up to 1024 shades of gray. The effective wavelength range of this system is from 200 nm to 840 nm. The spatial resolution depends on the distance of CCD camera from the central plane of shock tube, and is about 0.2 mm/pixel in the present experiment.

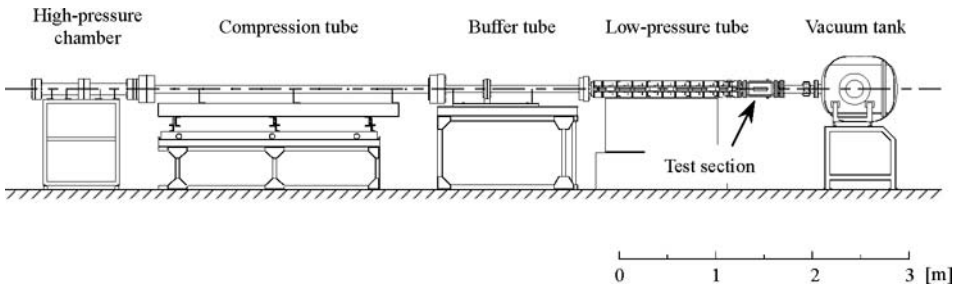

Fig. 1. Free-piston, double-diaphragm shock tube.

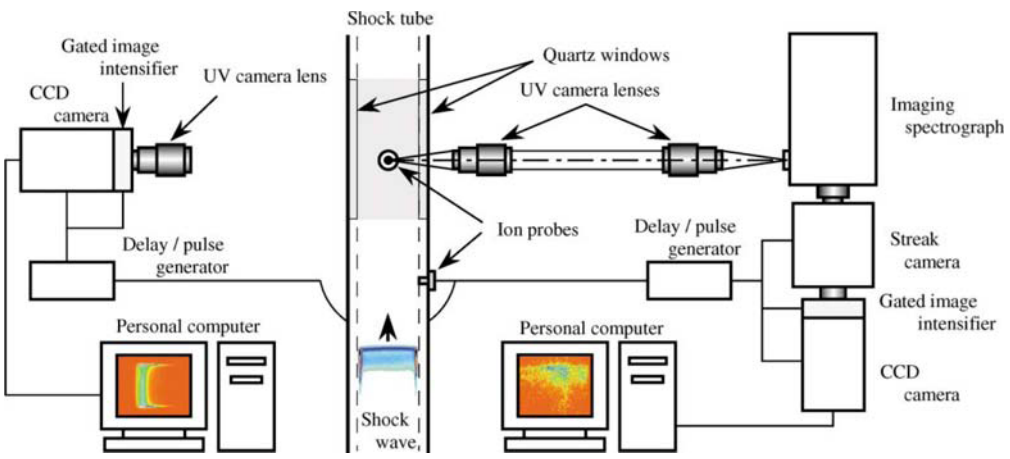

Fig. 2. Layout of diagnostic system.

The latter system consists of two UV camera lenses, an imaging spectrograph, a streak camera, an ICCD, a delay/pulse generator and a personal computer. The imaging spectrograph is a Chromex 500IS, focal length f = 500 mm with f/8 internal optics. This spectrograph is a one-pass, Czerny-Turner type. The reciprocal linear dispersion is 1.25 nm/mm. The entrance slit width is set to 100 μm throughout the observation. In order to get the space-resolved spectra, the streak camera is mounted at the exit plane of spectrgraph. The streak camera is a Hamamatsu Photonics, model C2830 with slow streak unit M2548 and a microchannel plate. The streak time (sweep speed) is set to 10 μs/15 mm. There is a horizontal slit of 10 mm length in the entrance optics, and the width in the present observation is set to 100 μm. The ICCD is mounted at the focal exit of streak camera. This ICCD consists of a gated image intensifier (I.I.), Hamamatsu Photonics, model C2925 and a CCD camera, Hamamatsu Photonics, model C4742. The I.I. and CCD camera are connected by means of a customized optical fiber. The two-dimensional diode array is composed by 1000 × 1018 square pixels of 12 μm × 12 μm, each pixel producing up to 1024 shades of gray. This system has the same effective wavelength range as the former system. A space-dependent spectral image can be obtained with a 25 nm wavelength range and an 80 mm space-interval. The spectral and the spatial resolutions are, respectively, 0.028 nm/pixel and 0.08 mm/pixel. The spectral broadening of this system is measured using a mercury spectral line, and its FWHM (Full Width at Half Maximum) is approximately 0.4 nm. The spatial broadening is 0.667 mm for a shock wave of 10 km/s velocity.

The shock velocity is measured by using ion probes mounted on the side walls of shock tube. The signal of ion probe at the upstream side is also used as a trigger of overall diagnostic systems. Considering the delay times of delay/pulse generators, Stanford Research Systems, model DG535, at both sides of shock tube, one can obtain the spatial relationship between both images of the total radiation and its spectral radiation.

3. Total Radiation Profile

Figure 3 shows a total radiation profile behind strong shock wave in air, whose shock velocity U_s is 9.6 km/s at the initial pressure p_1 = 13.3 Pa. Figures 3(a) and 3(b) show, respectively, a time-frozen, total radiation image and the axial radiation intensity profiles.

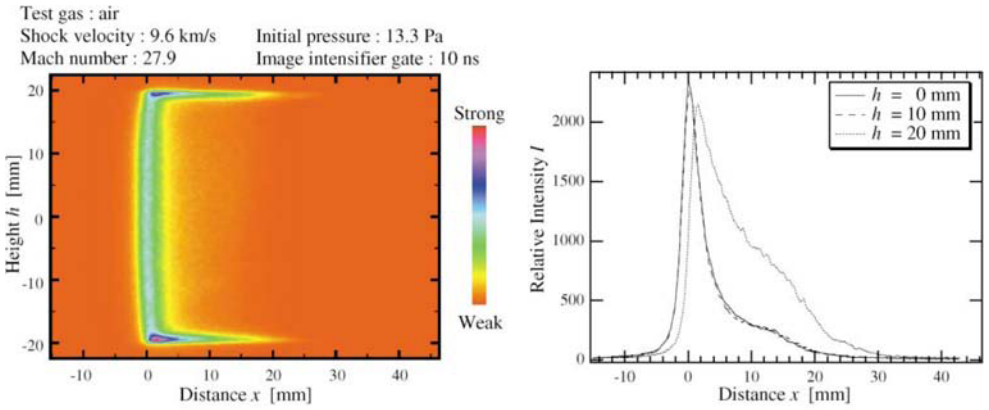

(a) Time-frozen, total radiation image. (b) Axial radiation intensity profiles.

Fig. 3. One-peak profile of total radiation intensity behind strong shock wave in air: U_s = 9.6 km/s, p_1 = 13.3 Pa.

In the total radiation image, the shock wave is propagating from right to left. The gate time of image intensifier is 10 ns. This small time-interval means that the image can be considered as time-frozen, since the movement of wave front in this interval is less than an order of 0.1 mm, whose distance is small enough compared with the width of radiation zone. The camera lense is focused on the central plane of shock tube. However, it is inevitable to take a radiation image integrated over the tube width for radiative gas with transparent nature. The resultant image exhibits a two-dimensional one integrated over the tube width in depth. The ordinate exhibits the height of tube inside, h in mm. The locations of h = ±20 mm are corresponding to the tube wall surfaces. The abscissa exhibits the distance of shock propagating direction, x in mm. The origin of abscissa is defined at the peak of total radiation profile along the tube axis of h = 0 mm just behind the shock front. The variety of color in the figure indicates degree of intensity shown by the bar on the right hand side in the image.

The radiation front is slightly curved in a convex form towards the negative direction of x-axis. This two- or three-dimensional behavior of radiation front is attributed to the curve of shock front itself, which is induced by the frictional effect on the tube wall surfaces. The radiation intensity along the tube wall surfaces is higher and its horizontal length is longer than those along the tube axis. As it will be described later in the present paper, it may be attributed to the effects of nonequilibrium boundary layer on the tube wall surfaces. From the axial profiles, it is found that the total radiation profiles within $h = \pm 10$ mm are almost the same. Namely, the total radiation profile around the tube axis can be considered as quasi-one-dimensional.

Figure 4 shows a total radiation profile for a higher velocity case, in which the shock velocity U_s is 11.6 km/s at the initial pressure $p_1 = 13.3$ Pa. The two-dimensional image and the axial profiles show that the radiation intensity along the tube axis reaches a secondary peak at $x = 5$ mm after a primary peak at $x = 0$ mm.

It is easily noted that the total radiation profiles along the tube axis in Figs. 3(b) and 4(b) are remarkably different from each other: the former has one peak, while the latter has two peaks. We call them as the 1-peak profile and the 2-peaks profile, respectively, and each peak as the first-peak and the second-peak in the case of 2-peaks profile. As the shock velocity increases above 11 km/s, the second-peak is formed, and the total radiation profile along the tube axis changes from the 1-peak profile to the 2-peaks profile.

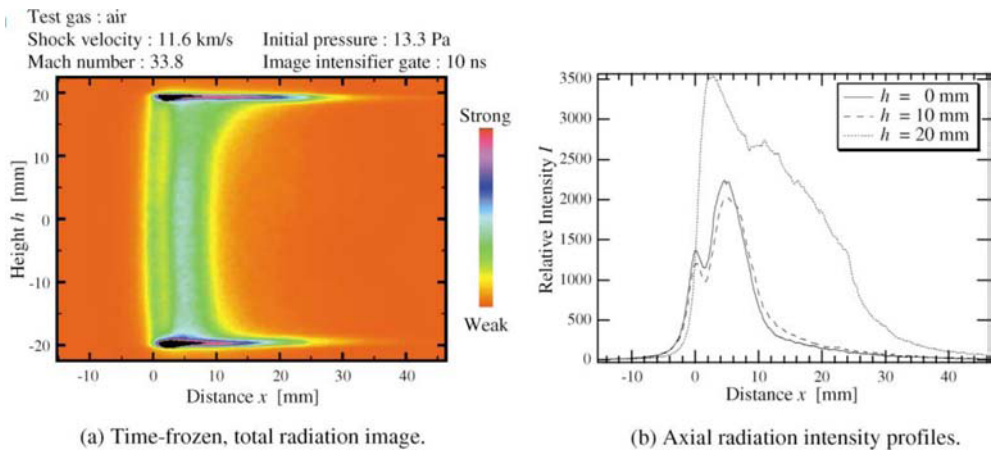

(a) Time-frozen, total radiation image. (b) Axial radiation intensity profiles.

Fig. 4. Two-peaks profile of total radiation intensity behind strong shock wave in air: $U_s = 11.6$ km/s, $p_1 = 13.3$ Pa.

4. Simultaneous Measurement for the Total Radiation and its Spectral Radiation

4.1 Radiation along the Tube Axis

The simultaneous observation for the total radiation and its spectral radiation along the tube axis are carried out by using the diagnostic system shown in Fig. 2, since it is necessary to elucidate the space-dependent contributions of the individual radiation spectrum to the total radiation intensity.

Figure 5 shows images obtained by the simultaneous observation for the shock velocity $U_s = 12.0$ km/s at the initial pressure $p_1 = 13.3$ Pa. The left- and right-hand side images exhibit, respectively, a time-frozen, total radiation image and a space-resolved, spectral radiation image. Unlike Figs. 3 and 4, the shock wave is propagating from bottom to top. After a time-resolved spectral image is obtained, the time is transformed to the distance by multiplying the shock velocity. Referred to the spatial relationship, both images are positioned to coincide with each other in the ordinate, i.e., the distance, x in mm, along the tube axis. The origin is fixed at a position where the total radiation profile along the tube axis exhibits a peak just behind the shock front. Each image is obtained independently with a relative intensity.

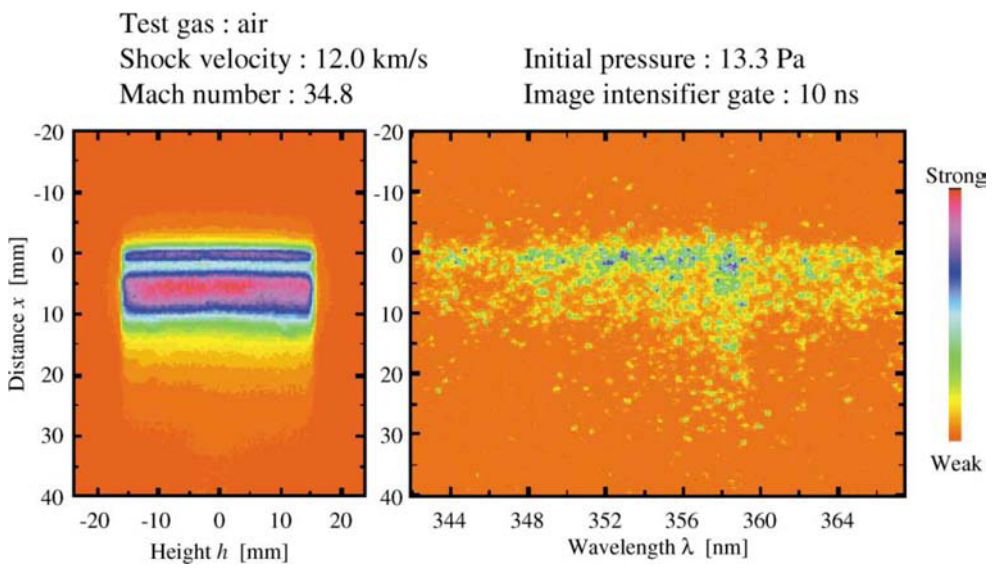

Fig. 5. Resultant images for total radiation (left) and its spectral radiation from 342 nm to 367 nm (right) in the case of the 2-peaks profile: U_s = 12.0 km/s, p_1 = 13.3 Pa.

In the total radiation image, the abscissa indicates the height of tube inside, h in mm. The radiation emission is cut off by shield sheets within 5 mm apart from both tube wall surfaces in order to observe the radiation around the tube axis with higher intensity resolution, since much stronger radiation is observed along the tube wall surfaces as previously shown in Figs. 3 and 4. From this image, the total radiation profile along the tube axis exhibits the 2-peaks profile, namely, the first-peak at x = 0 mm and the second-peak at x = 5 mm.

In the spectral radiation image, the abscissa indicates the wavelength, λ in nm. The wavelength range is selected from λ = 342 nm to λ = 367 nm to inquire into the spatial relationship between the total radiation and the spectral radiation due to the band spectra of N_2^+(1-) system, which are expected to appear at the wavelength range from λ = 350 nm to λ = 360 nm. As seen from this image, the spectra begins to emit at the same position with the first-peak of total radiation profile.

In order to elucidate more clearly the contribution of the spectral radiation to the total radiation intensity, the total radiation profile along the tube axis is compared with the spectral radiation profile along the tube axis, as shown in Fig. 6. Figures 6(a) and 6(b) correspond to, respectively, the cases of 1-peak profile (U_s = 9.8 km/s) and 2-peaks profile (U_s = 12.0 km/s) at the initial pressure p_1 = 13.3 Pa. The solid line indicates the total radiation profile, and the dotted line indicates the spectral radiation profile, which is obtained by integrating the radiation intensity over the wavelength range from λ = 350 nm to λ = 360 nm, including the band spectra of N_2^+(1-) system. Both profiles are normalized by their peak value just behind the shock front, as I/I_p.

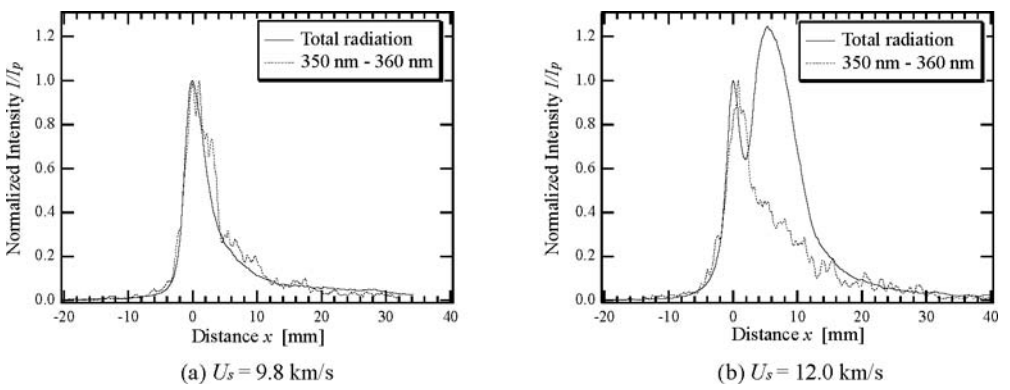

Fig. 6. Total radiation profile and spectral radiation profile including the band spectra of N_2^+(1-) system along the tube axis. Comparison between the cases of the 1-peak profile (a) and 2-peaks profile (b): p_1 = 13.3 Pa.

In the case of the 1-peak profile (a), the profile of the dotted line nearly coincides with the profile of the solid line. On the other hand, in the case of the 2-peaks profile (b), the dotted line does not coincide with the solid line. Although the second-peak is formed in the total radiation profile, the spectral radiation profile exhibits a gentle falling and any peak is not formed at the position of second-peak. Consequently, these results suggest us that the spectral radiation due to the band spectra of N_2^+(1-) system gives some contributions to the first-peak of total radiation profile for both cases of the 1-peak and 2-peaks.

Figure 7 shows the resultant images for a different wavelength range. In this case, the shock velocity U_s is 11.7 km/s at the initial pressure p_1 = 13.3 Pa. In the total radiation image, the total radiation profile along the tube axis exhibits the 2-peaks profile, although the intensity of second-peak is weaker than that of Fig. 5. In the spectral radiation image, the wavelength range is selected from λ = 412 nm to λ = 435 nm to inquire into the spatial relationship between the total radiation and the spectral radiations due to the band spectra of N_2^+(1-) system and the spectra of O^+, which are expected to appear at the wavelength range from λ = 412 nm to λ = 420 nm and the wavelength around λ = 434 nm. As clearly seen in this image, the former spectra concentrate around x = 0 mm at the first-peak, while the latter spectra concentrate around x = 5 mm at the second-peak. As for the spectra around λ = 434 nm, it should be noted that the H_γ spectral line of Balmer series can also appear around the same wavelength. The existence of hydrogen atoms and their spectra is confirmed by the fact that the H_β spectral line of Balmer series is also observed around x = 5 mm. Therefore, the spectra around λ = 434 nm will be referred to the spectra of O^+ and H_γ in the following. The hydrogen is considered to be included in the original test gas, which is the laboratory air.

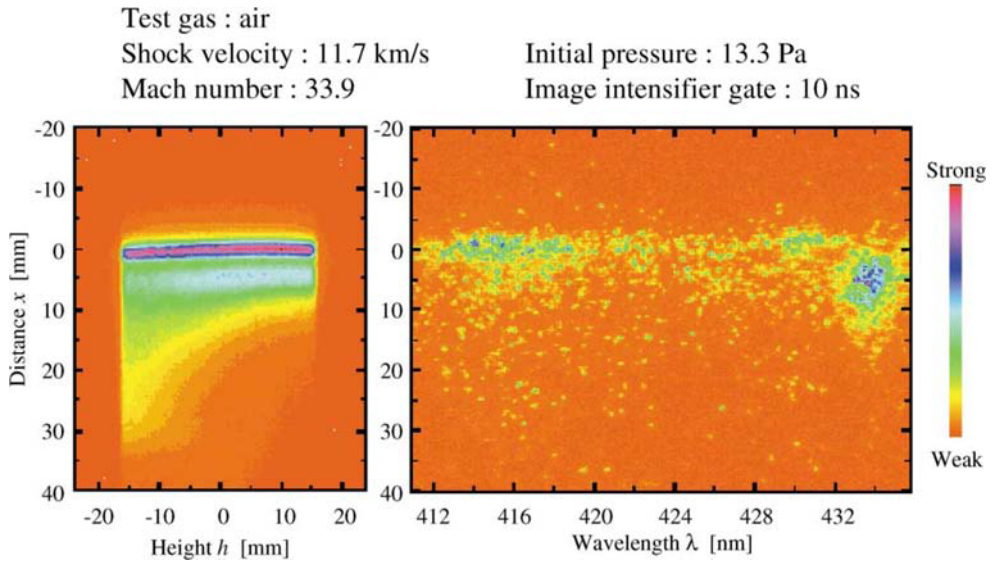

Fig. 7. Resultant images for total radiation (left) and its spectral radiation from 412 nm to 435 nm (right) in the case of the 2-peaks profile: U_s = 11.7 km/s, p_1 = 13.3 Pa.

Figure 8 shows the total radiation profile and the spectral radiation profiles along the tube axis for the 2-peaks. Figures 8(a) and 8(b) illustrate two cases, where the intensities of the second-peak relative to those of the first-peak are different from each other. The solid line indicates the total radiation profile. The dotted line indicates the spectral radiation profile, which is obtained by integrating the radiation intensity over the wavelength range from λ = 412.5 nm to λ = 417.5 nm, including the band spectra of N_2^+(1-) system. The dashed line indicates another spectral radiation profile, which is obtained by integrating the radiation intensity over the wavelength range from λ = 432 nm to λ = 435 nm, including the spectra of O^+ and H_γ. The intensities are also normalized by their peak values just behind the shock front for the solid and dotted lines. The peak value of the dotted line is also used as a reference value for the dashed line, in order to illustrate the relative intensities of integrated spectra of O^+ and H_γ to integrated band spectra of N_2^+(1-) system.

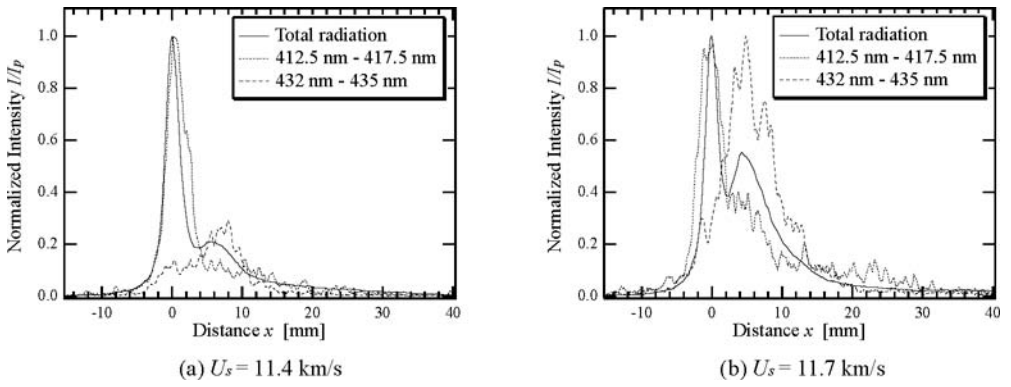

Fig. 8. Total radiation profile and spectral radiation profiles including the band spectra of N_2^+(1-) system and the spectra of O^+ and H_γ along the tube axis. Comparison between the cases of the 1-peak profile (a) and 2-peaks profile (b): p_1 = 13.3 Pa.

It should be noted that the peak positions of the dashed lines nearly coincide with the second-peak positions of the solid lines, while the peak positions of dotted lines nearly coincide with the first-peak positions of the solid lines. Furthermore, when the shock velocity increases, the relative magnitude of the peak of dashed line to the peak of dotted line increases in accordance with the tendency of the relative magnitude of the second-peak to the first-peak of total radiation profile. These results suggest us that the delayed spectra of O^+ and H_γ give some contributions to the formation of the second-peak of total radiation profile. On the other hand, the band spectra of N_2^+(1-) system contribute to the formation of the first-peak.

In order to inquire into the contribution of the spectra in each wavelength range to the total radiation, spectral observation is extended to the wider wavelength range. Figure 9 shows the resultant images for the shock velocity U_s = 12.1 km/s at the initial pressure p_1 = 13.3 Pa. The wavelength range is selected from λ = 302 nm to λ = 445 nm. This spectral radiation image is constructed from seven spectral radiation images obtained in different wavelength range. The total radiation image is one of the seven shots. In the seven shots, the shock velocities are reproducible within 0.6%.

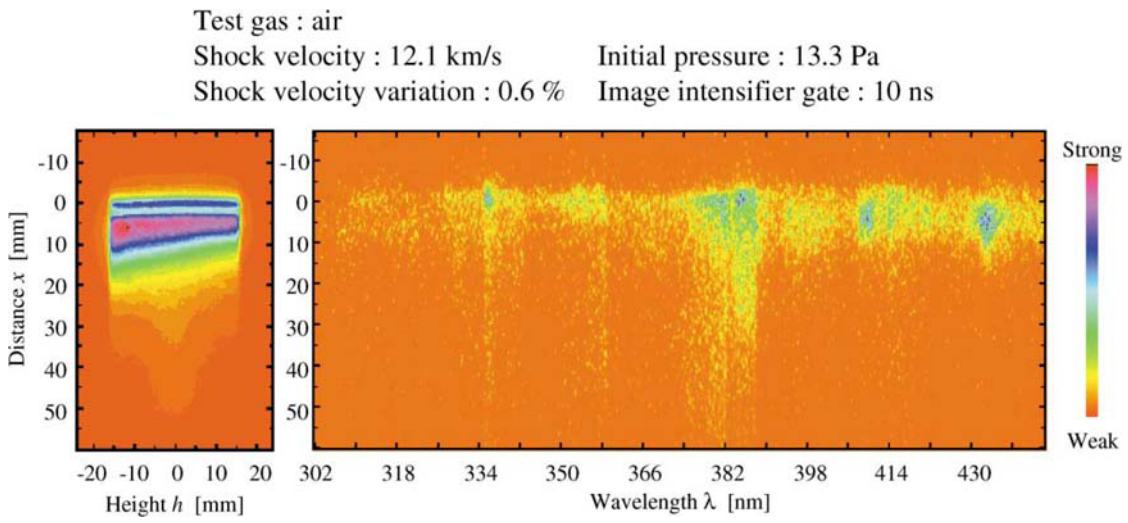

Fig. 9. Resultant images for total radiation (left) and its broadband spectral radiation from 302 nm to 445 nm (right): U_s = 12.1 km/s, p_1 = 13.3 Pa.

As seen from the total radiation image, the total radiation profile along the tube axis exhibits the 2-peaks profile. From comparison among these images, the spectral radiation in this wavelength range begins to emit nearly at the same position as the total radiation. However, it is found that the spectra around λ = 410 nm and λ = 434 nm appear at the same position with the second-peak.

Figure 10 shows the local interrelationship between an averaged total radiation profile (solid line) and four integrated spectral radiation profile (the other lines). Figures 10(a) and 10(b) correspond to the shock velocities of, respectively, U_s = 9.0 km/s and U_s = 12.1 km/s, which are chosen as typical cases of the 1-peak and the 2-peaks profiles of total radiation intensity. One spectral radiation profile is obtained by integrating the intensity over the 20 nm wavelength-interval in the spectral radiation image for a shot. Four different shots are needed to obtain four profiles, and then four total radiation profiles are obtained in the corresponding shots. The averaged total radiation in the figure means that the solid line is obtained by averaging the four profiles, for which the normalized intensity of the first-peak is commonly fixed at x = 0 mm. The experiments are carried out with good reproducibility in the shock velocity (0.6%) and the total radiation profile along the tube axis. The selected wavelength ranges are 342 nm ~ 362 nm, 362 nm ~ 382 nm, 402 nm ~ 422 nm and 422 nm ~ 442 nm, which include, respectively, the band spectra of N_2^+(1-) system, the band spectra of CNV system, the spectra of N and the band spectra of N_2^+(1-) system and the spectra O^+ and H_γ. Four spectral radiation profiles are normalized by a common value, i.e., the peak value of profile including the band spectra of CNV system.

In the case of 1-peak profile, i.e., in Fig. 10 (a), the spectral radiation profiles exhibit a similar form to each other in a look of steep rising and rather gentle falling. The contribution to the peak of total radiation profile can be considered to come from three wavelength ranges, except the profile of O^+ and H_γ with vanishing intensity. In particular, the profile of CNV system (green line) is considerably dominant, which may be attributed to the carbon impurities. It should be noted that there is a difference of the radiation rising between the profile of N_2^+(1-) system (red line) and the profile of N and N_2^+(1-) system (blue line). This difference may be attributed to the dissociative process of nitrogen molecules.

In case of 2-peaks profile, i.e., in Fig. 10(b), these four spectral profiles can be categorized into two types. Two profiles of shorter wavelength (red and green lines) exhibit the steep rising and the gentle falling of the radiation intensity, while two profiles of longer wavelength (blue and pink lines) exhibit the gentle rising and falling of radiation intensity. The former spectral radiation with shorter wavelength can be considered to contribute to the formation of first-peak of total radiation profile, since the peaks of spectral radiation profile are situated near at the first-peak (x = 0 mm). On the other hand, the latter spectral radiation with longer wavelength can be considered to contribute to the formation of second-peak of total radiation profile, since the peaks of spectral

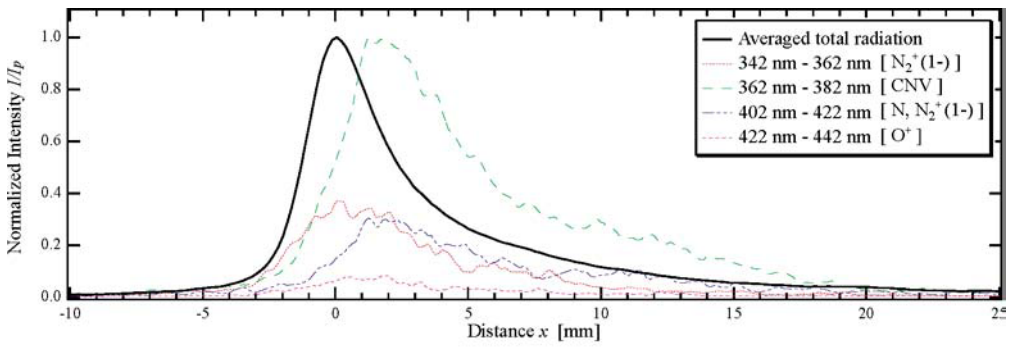

(a) U_s = 9.0 km/s (1-peak profile).

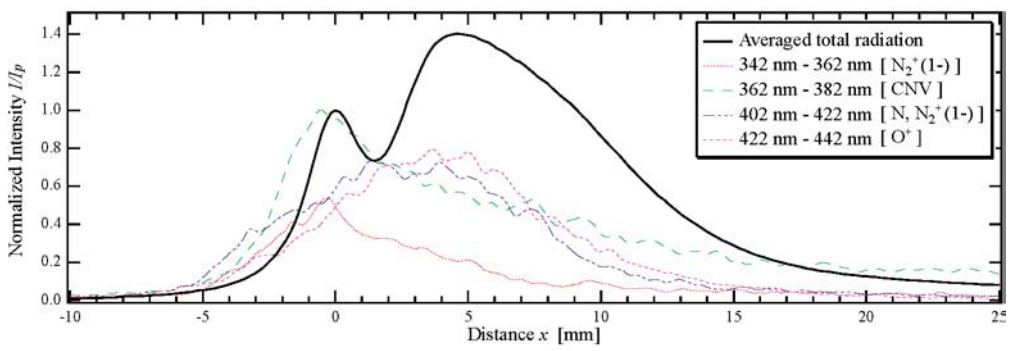

(b) U_s = 12.1 km/s (2-peaks profile).

Fig. 10. Local interrelationship among total radiation profile and its spectral radiation profiles along the tube axis Comparison between the cases of the 1-peak profile (a) and 2-peaks profile (b): p_1 = 13.3 Pa.

radiation profile are situated near at the second-peak (x = 5 mm). The steep falling of intensity near the peak in the shorter wavelength case also contributes to the formation of valley between the first-peak and the second-peak.

The spectra at the first-peak and the second-peak obtained from Fig. 9 are shown in Fig. 11, in order to look at their detailed constituents in the case of 2-peaks profile of total radiation intensity. The black and red lines exhibit the spectra centered at, respectively, the first-peak (x = 0 mm) and the second-peak (x = 5 mm) of the total radiation profile, and integrated for 2 mm space-interval. As seen from these spectra, the band spectra of N_2^+(1-) and CNV systems are distinctive around the first-peak. On the other hand, around the second-peak, the intensities of spectra of N, O^+ and H become relatively strong, while the intensities of band spectra of molecular species become relatively weak.

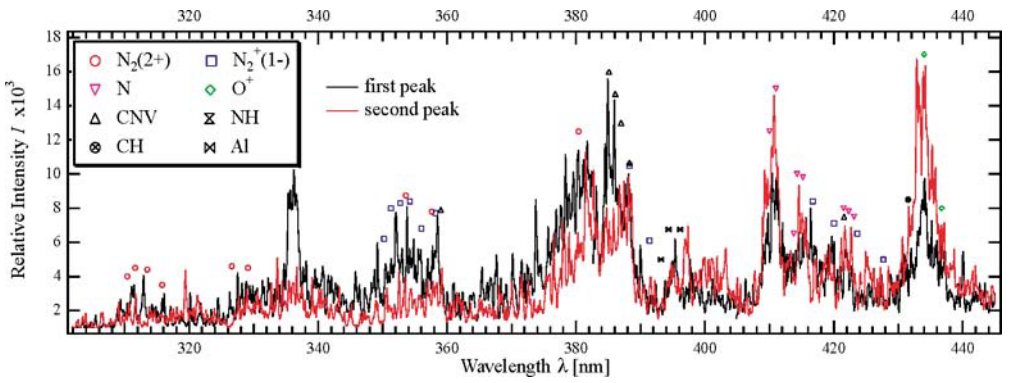

4.2 Radiation along the Tube Wall Surface

As shown in Figs. 3 and 4, much stronger and longer radiation is observed along the tube wall surfaces. Due to the previous conclusions by Keck et al. (1959) and Honma and Iizuka (1991), the radiation was attributed to the impurities coming from Na and K. In order to inquire exactly into the constituent, the simultaneous observation is carried out along the tube wall surface. In this observation, the system of space-resolved spectral radiation, which is shown on the right hand side in Fig. 2, is focused on a point of 0.5 mm apart from the tube wall surface.

Figure 12 shows the total radiation profiles and the spectral radiation profile. The solid and dashed lines exhibit the total radiation profile and the spectral radiation profile along the tube wall surface, respectively. For comparison, the total radiation profile along the tube axis is plotted by the dotted line. The spectral radiations in

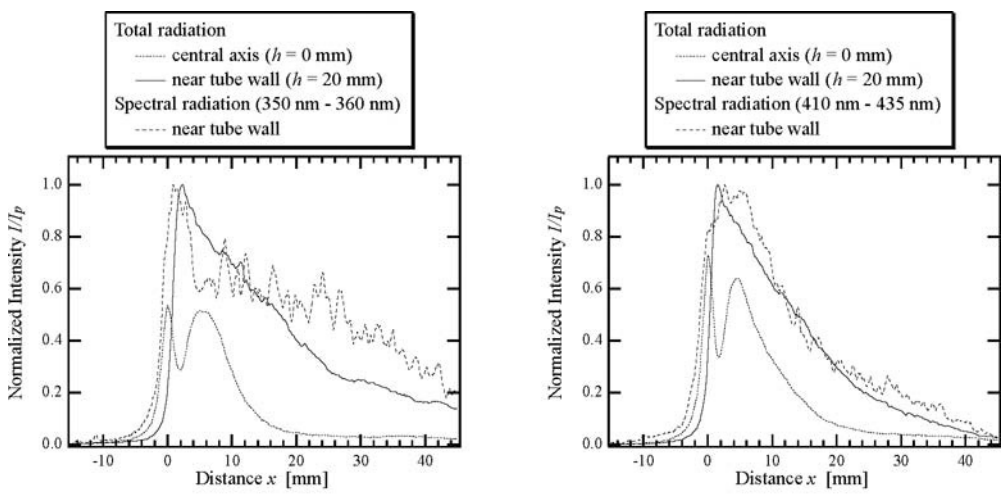

Fig. 12. Comparisons between the total radiation profiles and its spectral radiation profile along the tube wall: (a) U_s = 11.8 km/s, p_1 = 13.3 Pa; (b) U_s = 12.4 km/s, p_1 = 13.3 Pa.

Figs. 12(a) and 12(b) are integrated over the wavelength ranges from λ = 350 nm to λ = 360 nm and from λ = 410 nm to λ = 435 nm, respectively, which include the band spectra of N_2^+(1-) system, and the spectra of N, O^+ and H_γ and the band spectra of N_2^+(1-) system. In both cases, the total radiation profiles along the tube axis exhibit 2-peaks profile. However, the total radiation profiles along the tube wall surface are different from them, and exhibit the long and gentle falling. It should be noted that both spectral radiation profiles exhibit the same profiles as the total radiations along the tube wall surface.

In the present observation, the spectra of Na emitted around λ = 589 nm are also observed. However, it is overlapped by the continuum radiation, and is weaker than the spectra as described above. Therefore, it is difficult to consider whether the spectra of Na or K mainly contribute to the stronger and longer radiation along the tube wall surfaces. Consequently, it is found that the constituents of radiation along the tube wall surfaces are almost the same as those of radiation along the tube axis. We consider that the radiation may be attributed to the effects of nonequilibrium boundary layer on the tube wall surface. Although the radiation images are integrated over the tube width for radiative gases with transparent nature, it cannot be observed the effects of boundary layer from the profile along the tube axis. Thus, we expect that the boundary layer is considerably thin.

5. Conclusion

Nonequilibrium radiation phenomena behind strong shock wave in low-density air is observed by using a couple of CCD camera systems in the shock tube experiment. The simultaneous observations for the total radiation and its spectral radiation are carried out in order to elucidate the space-dependent contributions of an individual radiation spectrum to the total radiation intensity. It is found that the band spectra due to the molecular species N_2^+ and CN mainly contribute to the first-peak, while the spectra due to the atomic species O^+ and N mainly contribute to the formation of the second-peak. It is also found that the Balmer series in H spectra strongly contributes to the second-peak. The radiation along the tube wall surfaces is composed of the same constituents as those around the tube axis as well as the spectra coming from the impurities, and may be attributed to the effects of nonequilibrium boundary layer on the tube wall surfaces, which is considerably thin.

The present results by the coupled use of a pair of CCD camera systems provide the more detailed and useful information on nonequilibrium radiation phenomena. From a viewpoint of flow visualization, the present study exhibits an up-to-date of the CCD camera system for spectroscopy on hypervelocity flow phenomena.

Acknowledgment

The financial assistance received from the Japan Society for the Promotion of Science and the Ministry of Education, Science and Culture of Japan under Grant-in-Aids for Scientific Research 09305064 is acknowledged with thanks.

References

Dumitrescu, M. P., Ramjaun, A., Chaix, A., Pilverdier, H., Martin, R. and Brun, R., Time-Resolved Emission Spectroscopy of CN and C_2 Electronic Bands Behind a Strong Shock Waves in Planetary Atmospheres, Proceedings of 21st International Symposium on Shock Waves, I (1997), Houwing, A. F. P. et al. (eds), 251-255.

Fujita, K., Suzuki, K. and Abe, T., Air Radiation Analysis of Super-Orbital Reentry Vehicle, AIAA Paper, AIAA 97-2561 (1997-6).

Fujita, K., Sato, S., Abe, T. and Ebinuma, Y., Experimental Investigation of Air Radiation from Behind a Strong Shock Wave, AIAA Paper, AIAA 98-2467 (1998-6).

Honma, H., Shock Tube Studies of Strong Shock Waves, Proceedings of International Symposium on Aerospace and Fluid Science, in commemoration of the 50th anniversary of IFS, Tohoku University, Sendai (1993-11), 128-148.

Honma, H., Maeno, K., Morioka, T., Matsuura, Y. and Koreeda, J., Observation of Radiation Behind Strong Shock Waves in Air, Theoretical and Applied Mechanics, 45 (1996), Yagawa, G. and Ohtsubo, H. (eds), 231-239.

Honma, H. and Iizuka, H., Experimental and Numerical Studies of Radiation Emission from High-Temperature Air Behind 10 km/s Shock Waves, SAE Technical Paper Series 912025, reprinted from International Pacific & Space Technology Conference and 29th Aircraft Symposium Proceedings, Gifu, Japan, (1991).

Keck, J. C., Camm, J. C., Kivel, B. and Wentink, T. J., Radiation from Hot Air Part II: Shock Tube Study of Absolute Intensities, Annals of Physics, 7 (1959), 1-38.

Koreeda, J., Ohama, Y. and Honma, H., Time-Resolved Imaging Spectroscopy of Nonequilibrium Shock-Front Radiation in Air, Proceedings of 20th International Symposium on Shock Waves, Sturtevant, B. et al. (eds), Pasadena, USA (1996), 1181-1186.

Koreeda, J., Ohama, Y. and Honma, H., Imaging Spectroscopy of the Nonequilibrium Shock Front Radiation in Air, Shock Waves, Springer Verleg, 8 (1998), 71-78.

Morioka, T., Sakurai, N., Maeno, K. and Honma, H., Imaging Spectroscopy of Radiation Behind Strong Shock Waves in Air, Theoretical and Applied Mechanics, 46 (1997), Yagawa, G. and Miki, C. (eds), 307-315.

Sharma, S. P., Research on Nonequilibrium Phenomena at Ames E.A.S.T. Facility, Proceedings of 19th International Symposium on Shock Waves, Brun, R. et al. (ed), Marseille, France (1994), 241-248.

Sharma, S. P. and Gillespie, W. D., Nonequilibrium and Equilibrium Shock Front Radiation Measurements, Journal of Thermophysics and Heat Transfer, 5-3 (1991), 257-265.

Author Profile

Toshihiro Morioka: He received his BSc (Eng) degree in mechanical engineering in 1993 from Faculty of Engineering, Chiba University, and his Doctor of Engineering in production engineering in 1998 from Chiba University. He started his research career as a research fellow of the Japan Society for the Promotion of Science in 1997, and has worked as a research associate at Chiba University since 1998. His research interests include shock waves, high-temperature gas dynamics and computational fluid dynamics.

Nariaki Sakurai: He received his BSc (Eng) degree in mechanical engineering in 1996 from Faculty of Engineering, Chiba University, and his Master of Engineering in electronics and mechanical engineering in 1998 from Chiba University. He has worked at the Tokyo Electric Power Company, Inc., since 1998.

Kazuo Maeno: He received his BSc (Eng.) degree in aeronautics in 1974 from Faculty of Engineering, University of Tokyo, and his Doctor of Engineering in aerospace engineering in 1979 from the University of Tokyo. After taking the Doctor, he started his research career as a research associate at Tokyo Metropolitan College of Aeronautical Engineering. In 1981 he moved to Muroran Institute of Technology as an associate professor, then from 1990 he has worked as an associate professor at Chiba University. During the current position, he was an invited researcher of CNRS-Marseille (University of Marseille II) in 1993. His research interests cover shock waves, supersonic and hypersonic gasdynamics, multiphase fluid dynamics in cryogenic range, high power gas lasers and laser applications, and multi-dimensional flow field visualization.

Hiroki Honma: He received his BSc (Eng) degree in aeronautical engineering in 1959 from Faculty of Engineering, University of Tokyo, and his Doctor of Engineering in aerospace engineering in 1971 from University of Tokyo. He started his research career as an assistant at Aeronautical Research Institute, University of Tokyo, in 1959, and then has worked as a lecturer, an associated professor, and a professor at Chiba University since 1965, except one year term as a visiting professor at Institute of Aerospace Sciences, University of Toronto, from 1979 to 1980. His research interests include rarefied and high-temperature gas dynamics, shock wave technology and computational fluid dynamics.